Los Alamos National Laboratory is operated by the University of California for the United States Department of Energy under contract W-7405-ENG-36.

Calculation of Terrestrial Gamma-Ray Fields in Airborne Radiometric Surveys

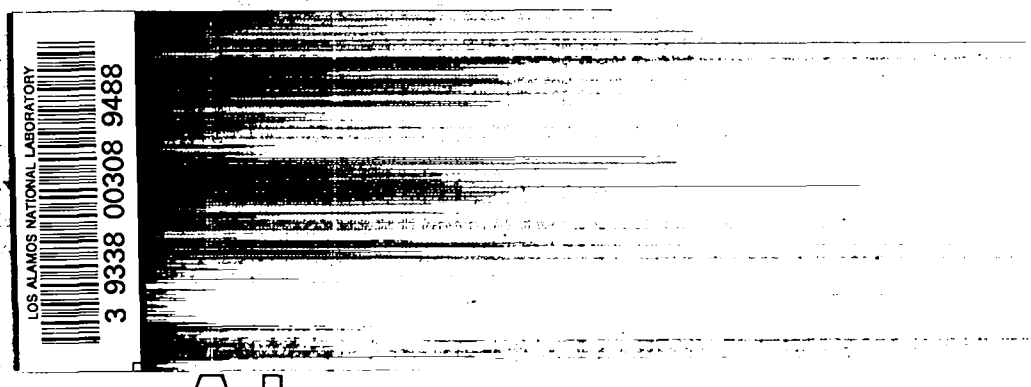

Los Alamos National Laboratory
Los Alamos, New Mexico 87545

This work was supported by the US Department of Energy, Division of Uranium Resources and Enrichment.

Prepared by Sophia Howard, Group Q-1

LA-9741-MS

UC-51
Issued: July 1983

Calculation of Terrestrial Gamma-Ray Fields in Airborne Radiometric Surveys

Michael L. Evans*

*3111 Meadowlane, Missouri City, TX 77459.

Los Alamos National Laboratory
Los Alamos, New Mexico 87545

CONTENTS

CALCULATION OF TERRESTRIAL GAMMA-RAY FIELDS IN AIRBORNE RADIOMETRIC SURVEYS

by

Michael L. Evans

ABSTRACT

Terrestrial gamma-ray fields have been calculated for points in air above semi-infinite rock formations containing known concentrations of the naturally occurring radionuclides ^{40}K, ^{235}U, ^{238}U, ^{232}Th, and their daughter products. Energy- and angle-dependent gamma-ray fluxes were computed using a discrete ordinates transport code. The density and composition of the rock medium as well as the air density and survey height were varied to determine their effect on the observed gamma-ray flux spectrum. Variations in formation porosity or water saturation cause little spectral shape perturbation above 200 keV and result chiefly in a scalar change that is related to the mass-density-weighted average $\overline{Z/A}$ of the rock formation. Corrections to the flux spectra for variations in air density and surface elevation can be made by simple scaling with density/altitude. However, the spectral shape of the observed gamma-ray flux depends strongly on the survey height above the rock/air interface, so that spectral stripping parameters must be determined as functions of survey height.

---

quantitatively understood. This situation has caused difficulties in the quantitative interpretation of gamma-ray spectral data. These calculations help establish the dependence of natural gamma-ray spectra on pertinent logging parameters and thereby provide a calculational basis for proper interpretation of the data.

Gamma-ray spectral surveys have become an important tool in uranium prospecting. Gamma rays from the naturally occurring radionuclides ^{40}K, ^{232}Th, ^{238}U, ^{235}U, and their daughter products give rise to a terrestrial radiation field that is quantified in field surveys by pulse-height spectra observed in scintillation detectors. In the potassium, uranium, and thorium (KUT) spectral method, windows are placed on the pulse-height spectrum, centered at the energies 1.461, 1.765, and 2.615 MeV, which include gamma rays characteristic of potassium, uranium, and thorium, respectively. The count rate observed in the windows is related to the concentration of these elements in the underlying rock formation. Downscattering of the higher energy gamma rays (primarily within the scintillator crystal) results in crosstalk among the channels that must be removed by spectral stripping methods if window count rates are to be proportional to the corresponding elemental concentrations in the formation. However, the stripping parameters used to unfold the pulse-height spectrum are dependent on many of the logging parameters, such as the density and composition of the formation, the presence or absence of overburden and/or vegetation cover, the air density and altitude at which the survey was taken, and the features of the ground/air interface.

In this study, energy and angular gamma-ray fluxes were computed at points in air above a rock formation having known abundances of potassium, uranium, and thorium. The density and composition of the rock medium as well as the air density and survey height were varied to determine their effect on the observed gamma-ray flux. Later computational studies could use these fluxes to determine the effect of variations in these and other logging parameters on the

pulse-height spectra (and consequently, the stripping parameters) observed in scintillation crystals of various sizes and shapes.[1]

II. MODEL DESCRIPTION

A. Geometry

The computational model used to simulate the emission and transport of terrestrial gamma radiation is shown schematically in Fig. 1. A plane interface separates two homogeneous, semi-infinite media. The rock or soil medium contains natural gamma-ray emitters uniformly distributed throughout the medium. The air medium is source free and its density is assumed constant with altitude above the rock surface. The one-dimensional discrete ordinates transport code ONETRAN[2] was used to compute angle- and energy-dependent fluxes at each spatial mesh point used in the model. These points lie along an altitude axis (Z-axis in Fig. 1) that is normal to the rock surface (Z = 0). The rock medium was made to look infinitely deep by using a 90-cm-thick rock layer and a reflective boundary. This configuration was deemed an adequate representation of an infinitely thick source region, because most of the radiation field observed at any altitude originates in the top 30 cm of the source-bearing rock medium.

The air medium was chosen to be 1.2802×10^5 cm (4200 ft) thick so that backscattering of gamma rays from air at the higher altitudes would be properly simulated for the highest altitude of interest in the calculation, that is, at 3.048×10^4 cm (1000 ft). The air medium was terminated by a vacuum boundary condition for the same reason. That is, use of an alternative boundary condition (such as a reflective boundary) would, in general, be equivalent to placing a source at high altitudes, resulting in erroneous angular flux distributions at all altitudes considered in the calculation. The model geometry chosen ensured that the flux calculated for the altitudes of interest would accurately reflect the true flux distribution.

B. Rock and Air Composition

Terrestrial gamma-ray fields have been computed for sandstone formations only, because earlier results from an infinite medium calculation[3,4] indicated that the changes in gamma-ray flux between shale and sandstone formations were small. The average elemental concentrations of dry, nonporous sandstone are

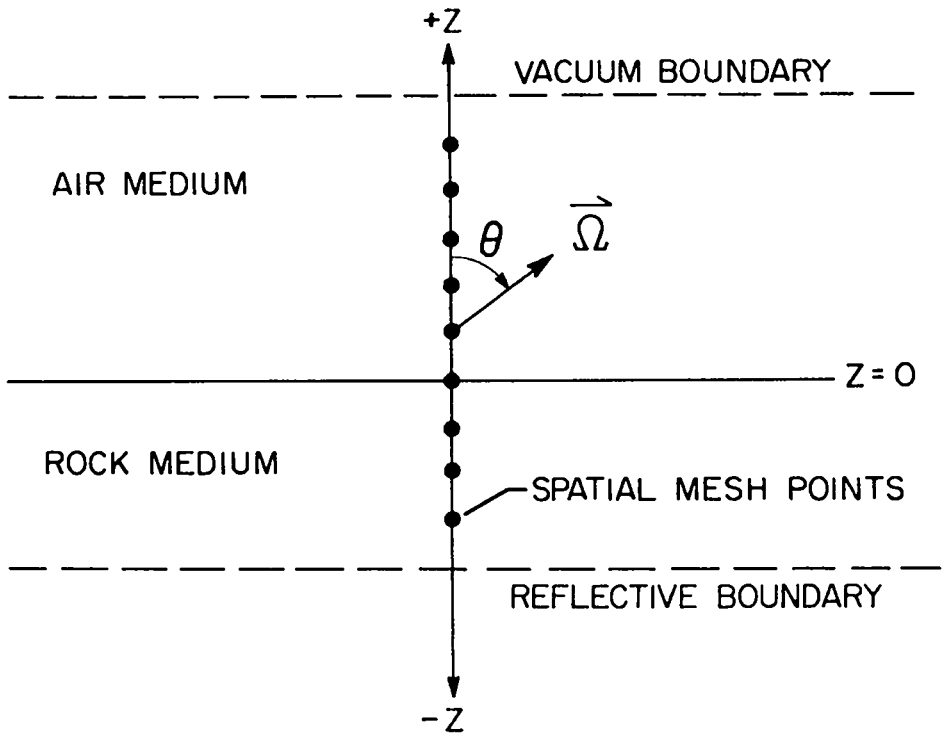

Fig 1. Model geometry used for the calculation of terrestrial gamma-ray fields.

given in Table I. This composition contains the eight most abundant constituents usually found in sandstones. Elements individually composing more than 0.4 wt% of the sandstone density (2.6263 g/cm^3) have been included. It will become apparent later that the omission of trace elements from the formation is not significant.

The presence of fluid in the rock formation is quantified by both rock porosity and the extent that the fluid saturates the pore spaces. When the effects of porosity and saturation are included, the bulk density ρ_B is related to the dry, nonporous rock density ρ_R as follows:

$$\rho_B = \rho_R (1 - P) + PS\rho_L \quad , \tag{1}$$

where

TABLE I

SANDSTONE ELEMENTAL CONCENTRATIONS[a]

Element	Mass Density (g/cm^3)	Weight Fraction (%)	Atom Fraction (%)
C	0.03661	1.394	2.337
O	1.37001	52.164	65.648
Mg	0.01880	0.716	0.593
Al	0.06700	2.551	1.904
Si	0.97399	37.086	26.587
K	0.02920	1.112	0.573
Ca	0.10450	3.979	1.999
Fe	0.02621	0.998	0.360

[a]Formation bulk density = 2.6263 g/cm^3; porosity = 0.0; saturation = 0.0; atom density = 0.07855 atoms/cm^3.

ρ_B = bulk density of the formation,

ρ_R = dry, nonporous rock density of the formation,

P = porosity, as a volume fraction,

ρ_L = formation fluid density (1.00 g/cm^3 for pure water), and

S = liquid saturation of the pore spaces, as a volume fraction.

The formation fluid was taken to be pure water, and the value of ρ_R used in the calculations did not include trace quantities of uranium or thorium present in the rock formation.

Gamma-ray spectral calculations were performed for the combinations of source porosity and saturation listed in Table II. All calculations except Case 10 assumed an air density corresponding to a sea-level rock/air interface (that is, ρ_{air} = 1.205 x 10^{-3} g/cm^3 at 15°C and 760 mm mercury). However, Case

10 was performed assuming a rock/air interface having an altitude of 8000 ft above sea level (that is, $\rho_{air} = 8.95 \times 10^{-4}$ g/cm^3 at -0.8°C and 564 mm mercury).

The air medium used in the calculations was assumed to be constant in density for all points above the formation surface. The air was composed of 76.8 wt% nitrogen and 23.2 wt% oxygen. Minor constituents normally found in air were not included because of the very small effect their inclusion would have on the computed gamma-ray fluxes.

TABLE II

INDEX TO THE PARAMETERS OF THE TERRESTRIAL GAMMA-RAY CALCULATIONS

Case	Gamma-Ray Source	Porosity	Saturation	Bulk Density (g/cm^3)
1	K	0.3	0.0	1.8384
2	K	0.3	0.5	1.9884
3	K	0.3	1.0	2.1384
4	U	0.3	0.0	1.8384
5	U	0.3	0.5	1.9884
6	U	0.3	1.0	2.1384
7	Th	0.3	0.0	1.8384
8	Th	0.3	0.5	1.9884
9	Th	0.3	1.0	2.1384
10	Th	0.3	0.5	1.9884[a]
11	Th	0.1	0.5	2.4137
12	Th	0.2	0.5	2.2011

[a]The air density for Case 10 was taken to be that corresponding to an altitude of 2.4384 x 10^5 cm (8000 ft) above sea level ($\rho_{air} = 8.95 \times 10^{-4}$ g/cm^3 at 0-8°C and 564 mm mercury).

C. Gamma-Ray Source Spectra

Separate calculations were performed for the gamma-ray spectra from the naturally occurring radioactive isotopes ^{40}K, ^{235}U, ^{238}U, and ^{232}Th. The gamma-ray energies and intensities for the uranium and thorium decay series and the decay of ^{40}K are listed in Tables III through V and presented graphically in Fig. 2. The source spectra were compiled from recently obtained nuclear decay data.[5-7] The absolute intensities have been normalized to 100 disintegrations of the parent nucleus assuming secular equilibrium of the uranium and thorium decay series. The absolute intensities of the ^{235}U decay series were normalized to 100 disintegrations of ^{238}U by assuming an isotopic ratio $^{235}U/^{238}U = 0.007253$. The gamma-ray lines have been ordered according to decreasing energy.

Because the uranium and thorium series contain many gamma-ray lines, the source spectra have been limited to those lines with intensities greater than or equal to 0.1 gamma rays/100 disintegrations of the parent nucleus. This arbitrary cutoff has little effect on the accuracy of computed pulse-height distributions because relatively large windows containing many source lines are used in KUT spectral logging.

The energy-dependent gamma-ray fluxes were computed for 261 energy bins having 10-keV width and spanning the range 10 keV-2.62 MeV to include the most energetic source gamma ray of interest--the 2.6145-MeV line from ^{208}Tl in the thorium series. Because the energy resolution of the calculations is 10 keV, instances occur in which more than one line lies within the same energy group and is unresolvable by the computer code. In these cases (indicated by brackets in Tables IV and V), the intensity of the energy group is taken to be the sum of the individual gamma-ray line intensities.

The calculated gamma-ray spectral fluxes can be assigned absolute values given the dry weight bulk density of the formation and the specific activity of each parent nuclide (that is, ^{40}K, ^{238}U, and ^{232}Th). The specific activities of these nuclides are taken to be

potassium 2.650×10^5 dis/s/g ^{40}K ,

uranium 1.244×10^4 dis/s/g ^{238}U ,

and

thorium 4.058×10^3 dis/s/g ^{232}Th .

TABLE III

GAMMA-RAY SOURCE SPECTRUM
FOR POTASSIUM

Energy (keV)	Intensity (Gamma Rays/100 dis ^{40}K)	Excited Nucleus
1460.8	10.67	^{40}Ar
511.0	0.002	^{40}Ar

TABLE IV

GAMMA-RAY SOURCE SPECTRUM
FOR URANIUM

Energy[a] (keV)	Intensity (Gamma Rays/100 dis ^{238}U)	Excited Nucleus
2447.8	1.54	^{214}Po
2293.4	0.32	^{214}Po
2204.2	4.99	^{214}Po
2118.6	1.19	^{214}Po
1896.3	0.18	^{214}Po
1873.2	0.23	^{214}Po
1847.4	2.10	^{214}Po
1838.4	0.38	^{214}Po
1764.5	15.80	^{214}Po
1729.6	2.98	^{214}Po
1684.0	0.24	^{214}Po
1661.3	1.15	^{214}Po
1599.3]	0.33	^{214}Po
1594.7]	0.27	^{214}Po
1583.2	0.72	^{214}Po
1543.3	0.35	^{214}Po
1538.5	0.41	^{214}Po
1509.2	2.19	^{214}Po

[a]Brackets indicate energies whose intensities were summed before input into ONETRAN.

TABLE IV
(cont)

GAMMA-RAY SOURCE SPECTRUM
FOR URANIUM

Energy (keV)	Intensity (Gamma Rays/100 dis ^{238}U)	Excited Nucleus
1408.0	2.48	^{214}Po
1401.5	1.39	^{214}Po
1385.3	0.78	^{214}Po
1377.7	4.05	^{214}Po
1303.8	0.12	^{214}Po
1281.0	1.47	^{214}Po
1238.1	5.95	^{214}Po
1207.7	0.46	^{214}Po
1155.2	1.69	^{214}Po
1133.7	0.26	^{214}Po
1120.3	15.04	^{214}Po
1070.0	0.29	^{214}Po
1052.0	0.32	^{214}Po
1001.2	0.59	^{234m}Pa
964.1	0.38	^{214}Po
934.1	3.19	^{214}Po
904.3	0.11	^{214}Po
839.2	0.59	^{214}Bi
831.8	0.16	^{211}Bi
821.2	0.15	^{214}Po
806.2	1.23	^{214}Po
786.1	0.31	^{214}Po
786.0	0.86	^{214}Bi
768.4	4.91	^{214}Po
766.6	0.21	^{234m}Pa
752.8	0.13	^{214}Po
719.9	0.40	^{214}Po
703.1	0.47	^{214}Po
665.5	1.56	^{214}Po

TABLE III

GAMMA-RAY SOURCE SPECTRUM
FOR POTASSIUM

Energy (keV)	Intensity (Gamma Rays/100 dis ^{40}K)	Excited Nucleus
1460.8	10.67	^{40}Ar
511.0	0.002	^{40}Ar

TABLE IV

GAMMA-RAY SOURCE SPECTRUM
FOR URANIUM

Energy[a] (keV)	Intensity (Gamma Rays/100 dis ^{238}U)	Excited Nucleus
2447.8	1.54	^{214}Po
2293.4	0.32	^{214}Po
2204.2	4.99	^{214}Po
2118.6	1.19	^{214}Po
1896.3	0.18	^{214}Po
1873.2	0.23	^{214}Po
1847.4	2.10	^{214}Po
1838.4	0.38	^{214}Po
1764.5	15.80	^{214}Po
1729.6	2.98	^{214}Po
1684.0	0.24	^{214}Po
1661.3	1.15	^{214}Po
1599.3	0.33	^{214}Po
1594.7	0.27	^{214}Po
1583.2	0.72	^{214}Po
1543.3	0.35	^{214}Po
1538.5	0.41	^{214}Po
1509.2	2.19	^{214}Po

[a]Brackets indicate energies whose intensities were summed before input into ONETRAN.

TABLE IV
(cont)

GAMMA-RAY SOURCE SPECTRUM
FOR URANIUM

Energy (keV)	Intensity (Gamma Rays/100 dis ^{238}U)	Excited Nucleus
241.9	7.60	^{214}Bi
236.0	0.50	^{223}Ra
234.6	0.16	^{223}Ra
205.3	0.21	^{231}Th
186.2	3.30	^{222}Rn
185.7	2.49	^{231}Th
163.4	0.21	^{231}Th
154.3	0.26	^{219}Rn
144.3	0.15	^{219}Rn
143.8	0.48	^{231}Th
112.8	0.24	^{234}Pa
92.8	2.67	^{234}Pa
92.4	2.70	^{234}Pa
78.9-86.0	23.8	X rays
84.2	0.30	^{231}Pa
80.0	0.37	^{223}Ra
67.7	0.37	^{226}Ra
63.3	3.80	^{234}Pa
53.3	0.12	^{230}Th
53.2	2.20	^{214}Bi
50.2	0.33	^{223}Ra
49.6	0.32	^{234}Th
46.5	4.05	^{210}Bi
27.3	0.32	^{227}Ac
25.6	0.60	^{213}Pa
10.8-11.7	26.1	X rays

TABLE V

GAMMA-RAY SOURCE SPECTRUM
FOR THORIUM

Energy[a] (keV)	Intensity (Gamma Rays/100 dis ^{232}Th)	Excited Nucleus
2614.5	35.93	^{208}Pb
1887.4	0.11	^{228}Th
1806.0	0.12	^{212}Po
1685.9	0.10	^{228}Th
1666.4	0.21	^{228}Th
1638.0]	0.54	^{228}Th
1630.4]	1.95	^{228}Th
1624.7]	0.32	^{228}Th
1620.6]	1.55	^{212}Po
1587.9]	3.71	^{228}Th
1580.2]	0.71	^{228}Th
1556.9	0.20	^{228}Th
1512.8	0.32	^{212}Po
1501.5	0.58	^{228}Th
1495.8	1.05	^{228}Th
1459.2	1.04	^{228}Th
1287.5	0.12	^{228}Th
1247.1	0.57	^{228}Th
1153.6	0.16	^{228}Th
1110.6	0.35	^{228}Th
1095.7]	0.13	^{228}Th
1094.0]	0.14	^{208}Pb
1078.8	0.54	^{212}Po
1065.1	0.15	^{228}Th
1033.1	0.23	^{228}Th
988.1	0.19	^{228}Th
968.9]	17.46	^{228}Th
964.6]	5.45	^{228}Th
958.5]	0.32	^{228}Th
952.1]	0.18	^{212}Po

[a]Brackets indicate energies whose intensities were summed before input into ONETRAN.

TABLE V
(cont)

GAMMA-RAY SOURCE SPECTRUM
FOR THORIUM

Energy (keV)	Intensity (Gamma Rays/100 dis ^{232}Th)	Excited Nucleus
948.0	0.12	^{228}Th
944.1	0.11	^{228}Th
911.1	29.00	^{228}Th
904.2	0.87	^{228}Th
893.4	0.37	^{212}Po
860.4	4.42	^{208}Pb
840.2	0.99	^{228}Th
835.6	1.82	^{228}Th
830.4	0.62	^{228}Th
794.8	4.84	^{228}Th
785.5	1.12	^{212}Po
782.0	0.55	^{228}Th
772.1	1.62	^{228}Th
763.1	0.65	^{208}Pb
755.2	1.10	^{228}Th
727.2	6.65	^{212}Po
727.0	0.80	^{228}Th
707.3	0.16	^{228}Th
701.5	0.20	^{228}Th
674.6	0.10	^{228}Th
651.3	0.10	^{228}Th
583.2	0.15	^{228}Th
583.1	130.90	^{208}Pb
572.1	0.16	^{228}Th
570.7	0.19	^{228}Th
562.3	0.99	^{228}Th
546.3	0.22	^{228}Th
523.0	0.12	^{228}Th
510.7	8.26	^{208}Pb

TABLE V
(cont)

GAMMA-RAY SOURCE SPECTRUM
FOR THORIUM

Energy (keV)	Intensity (Gamma Rays/100 dis ^{232}Th)	Excited Nucleus
509.6	0.49	^{228}Th
503.7	0.22	^{228}Th
478.2	0.24	^{228}Th
463.0	4.64	^{228}Th
452.8	0.36	^{208}Th
440.3	0.15	^{228}Th
409.4	2.23	^{228}Th
340.9	0.42	^{228}Th
338.4	12.01	^{228}Th
332.4	0.47	^{228}Th
328.0	3.50	^{228}Th and ^{208}Tl
321.7	0.25	^{228}Th
300.1	3.41	^{212}Bi
288.1	0.34	^{208}Tl
279.0	0.23	^{228}Th
277.4	2.48	^{208}Pb
270.3	3.77	^{228}Th
252.6	0.29	^{208}Pb
241.0	3.90	^{220}Rn
238.6	44.91	^{212}Bi
233.4	0.11	^{208}Pb
216.0	0.24	^{224}Ra
209.4	4.55	^{228}Th
204.1	0.17	^{228}Th
199.5	0.35	^{228}Th
191.5	0.12	^{228}Th
184.6	0.10	^{228}Th
154.2	0.99	^{228}Th
145.9	0.22	^{228}Th

by a normalization factor F given by

$$F = \rho_R P \lambda_s \times 10^{-6} \quad ,$$

where λ_s is the specific activity of the source (listed above for potassium, uranium, and thorium) and ρ_R and P are previously defined in Eq. (1). Alternatively, this activity corresponds to 32.26, 0.08039, and 0.2464 mg/cm^3 of potassium, uranium, and thorium, respectively, in the formation.

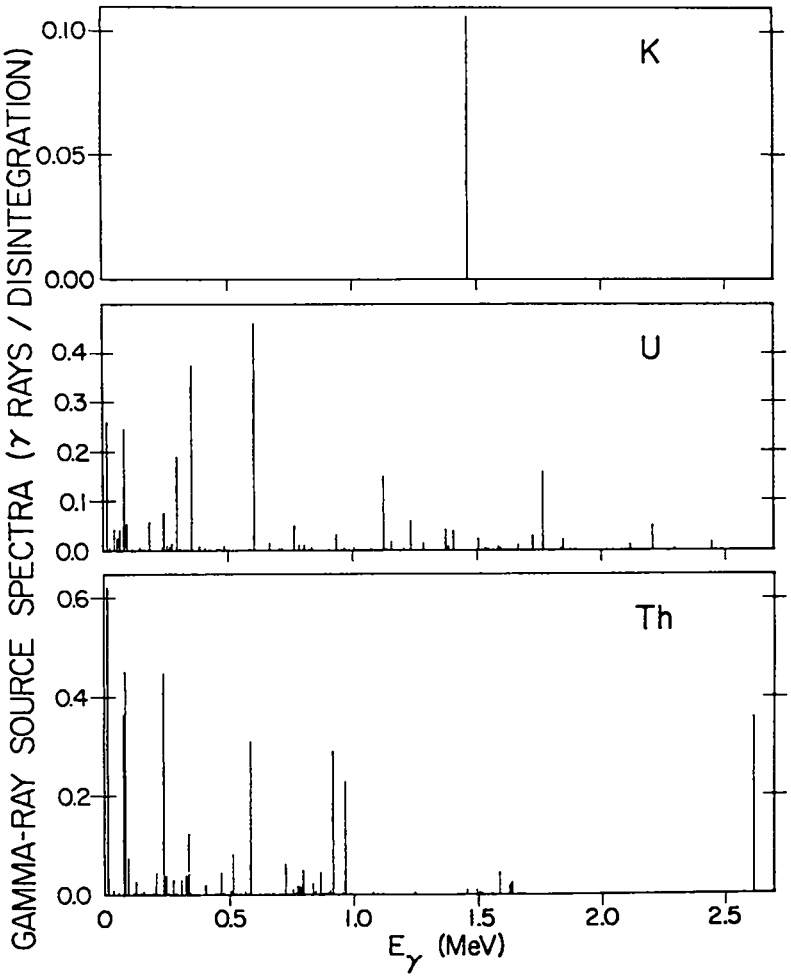

Fig. 2. Intensities of the gamma rays from the decay of ^{40}K, ^{235}U, ^{238}U, ^{232}Th, and their daughters assuming secular equilibrium. The intensities are normalized to one disintegration of the parent nucleus.

III. CALCULATION OF ANGULAR AND SCALAR FLUXES

A. Groundshine and Skyshine Flux Components

The one-dimensional discrete ordinates transport code ONETRAN was used to solve the Boltzmann equation for the two media of Fig. 1. Because the model assumes that the rock and air media are infinite in the x- and y-directions, the spectral radiation field will depend only on the coordinate z and the polar angle θ between the flux direction vector Ω and the Z-axis. That is, the angular flux $\Psi(z,\theta,E)$ will be constant in any horizontal plane and will be symmetric about any line normal to the rock/air interface. Thus, ψ will be

gent flux values. The accuracy of those values was independently verified by comparison with values computed using the Monte Carlo photon transport code MCG.[9] The MCG studies showed that the groundshine angular fluxes computed by ONETRAN were accurate to within ~1% (neglecting errors in the photon cross sections). This result is not surprising, because the groundshine fluxes consist chiefly of uncollided flux from the rock medium, so that the truncation of the cross-section expansion has little effect on the angular flux. In fact, the uncollided flux can be computed analytically for this simple geometry without resorting to transport methods. However, in general, the scattered radiation field is very complex even for this idealized geometry because gamma rays emitted by sources in the rock formation may suffer multiple scatterings in the rock and air.

The absence of sources in the air medium implies that the skyshine angular fluxes consist entirely of scattered radiation. It is not surprising that the skyshine flux is fairly accurate (~5%) at low gamma-ray energies, where the flux distribution is fairly isotropic and the scattering is adequately described by a low-order expansion of the cross sections. However, as the energy increases, the accuracy of the fluxes worsens as the low-order cross-section expansion becomes insufficient to describe accurately the extreme forward scattering dependence of the Compton cross section at higher energies (that is, 1-3 MeV).

Inaccuracies in the skyshine fluxes at high energies are of little concern if one considers the contribution of the skyshine flux to the total flux observed at a given altitude. The groundshine, skyshine, and total (groundshine

plus skyshine) fluxes at a point 0.3 m (1 ft) above the rock/air interface are shown in Figs. 3-5 for potassium, uranium, and thorium sources uniformly distributed in the rock medium with dry weight concentrations of 16.48%, 4.373 ppm, and 13.4 ppm, respectively. The spectra of groundshine flux are characterized by peaks of unscattered gamma rays from the source, whereas the skyshine flux consists of a continuum of scattered gamma rays except for the annihilation peak at 0.511 MeV caused by pair production events in the air. For thorium spectra, the skyshine flux is $\sim$0.1% of the total flux at 2.614 MeV, $\sim$0.4% at 1.588 MeV, and $\sim$1.2% at 0.583 MeV. Thus, for energies greater than about 1.5 MeV where the skyshine fluxes become relatively inaccurate, their contribution to the total flux is negligible.

B. Dependence of the Angular Flux on Energy and Height

The energy dependence of the angular flux $\psi(z,\theta,E)$ is shown in Figs. 6-8 at survey heights of 0.3 m (1 ft) and 122.9 m (400 ft). The flux is due to a 13.4-ppm thorium source uniformly distributed in the rock formation. As one might expect, the angular flux becomes more isotropic with decreasing energy at both heights. At the highest energy (2.61-2.62 MeV), the angular flux consists only of groundshine (mostly unscattered) gamma rays. However, as the energy decreases, gamma rays from the rock formation can downscatter from higher energies with large scattering angles producing the skyshine component and making the angular flux more isotropic. At 0.45-0.46 MeV, the skyshine contribution becomes a nonnegligible component of the total flux and is clearly discernible in Fig. 7. At low energies (90-100 keV), the skyshine component can become a significant contribution to the observed flux.

The variation of the angular fluxes at different survey heights is also evident from the figures. At any given energy, the angular flux becomes more forward peaked with increasing survey height. Greater heights favor gamma rays originating from sources directly beneath the observation point as compared with those starting some distance away. Gamma rays from these distant sources contribute little to the total flux because of increased absorption and decreased solid angle. Annular "circles of investigation"[10] can be defined on the interface beneath the observation point, each contributing a specific portion of the angular distribution. The influence of these circles of investigation on the dependence of the spectral flux on survey height will be discussed later (Sec. IV.B).

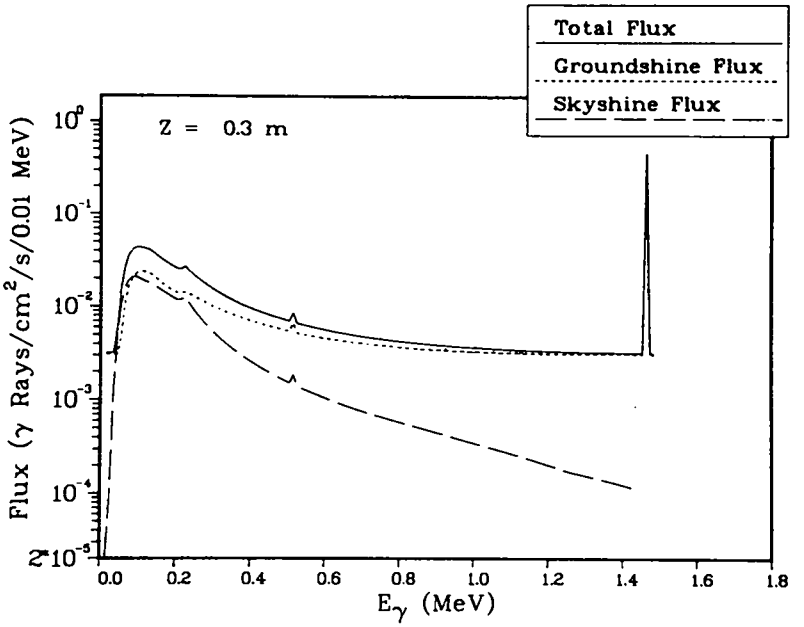

Fig. 3. Gamma-ray flux components at a survey height of 0.3 m (1 ft) for a potassium source having a dry weight concentration of 16.48%.

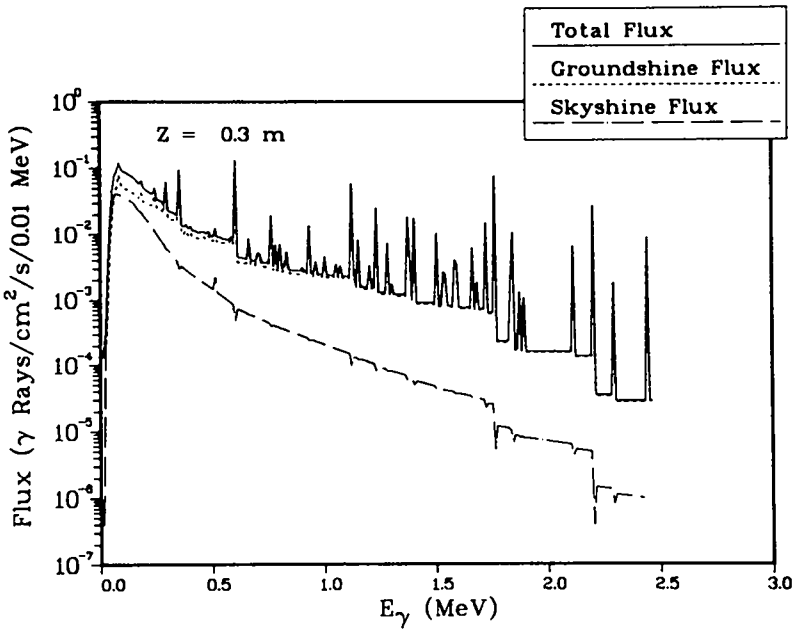

Fig. 4. Gamma-ray flux components at a survey height of 0.3 m (1 ft) for a uranium source having a dry weight concentration of 4.373 ppm.

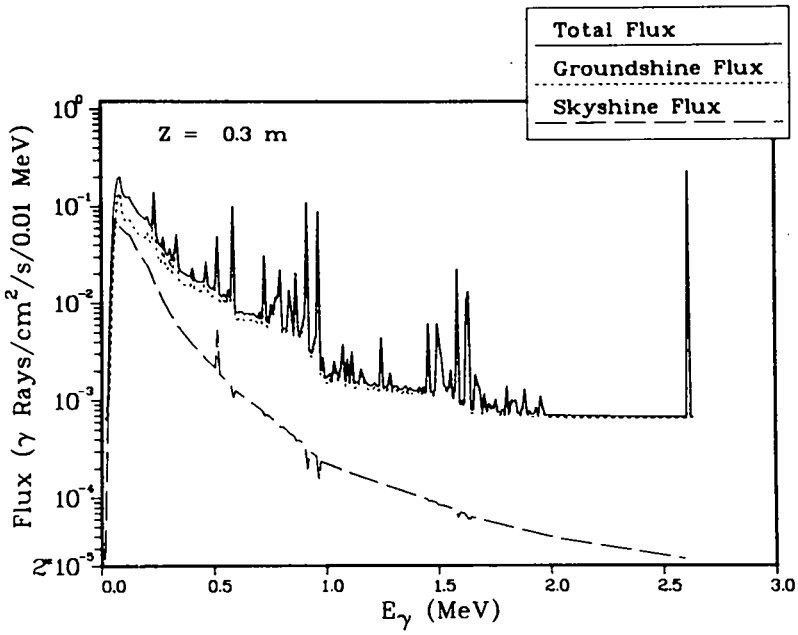

Fig. 5. Gamma-ray total, groundshine, and skyshine flux components at a survey height of 0.3 m (1 ft) for a thorium source having a dry weight concentration of 13.4 ppm.

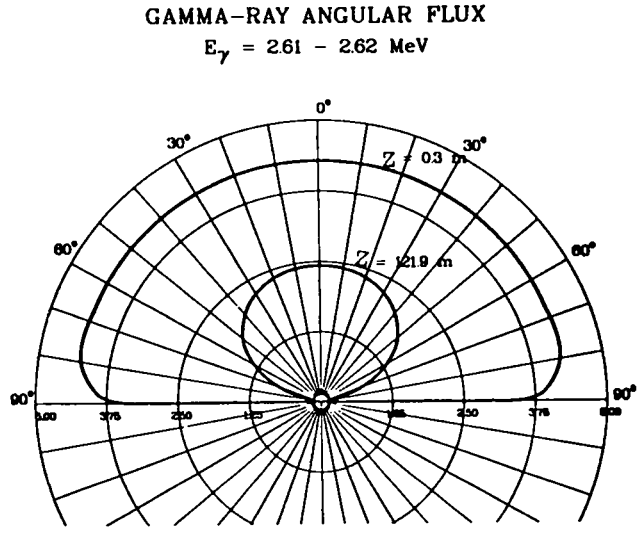

Fig. 6. Gamma-ray angular flux at survey heights of 0.3 m (1 ft) and 121.9 m (400 ft) for the 2.61-2.62-MeV energy bin resulting from a thorium source having a dry weight concentration of 13.4 ppm.

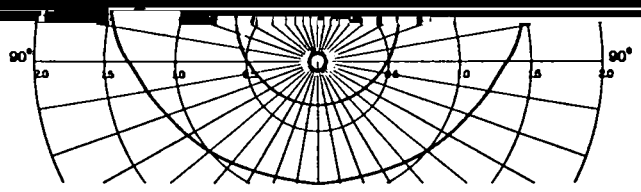

Fig. 8. Gamma-ray angular flux for the 0.09-0.10-MeV energy bin resulting from a 13.4-ppm thorium concentration in the rock medium.

IV. RESULTS

A. Dependence of the Total Flux on Formation Porosity, Saturation, and Density

Radiometric logging data are meaningful only if they can be related quantitatively to the response to calibration models having known radio-element concentrations, composition, density, etc. The logs must be corrected for differing formation composition and density as well as survey height, air density, radon background, etc. The corrected logs should then yield detector count rates that vary linearly with radio-element concentration in the formation.

The dependence of the total flux on formation porosity, water saturation, and density will be discussed only for the thorium source spectrum because that spectrum spans the energy range of both the potassium and uranium spectra. Thus, conclusions drawn from studying spectral shape changes for the thorium spectrum apply as well to the potassium and uranium spectra.

Ratios of the total flux from several different formations are shown in Figs. 9 and 10 as functions of gamma-ray energy. The total flux values are those at a point 0.3 m (1 ft) above the rock/air interface assuming a thorium dry weight concentration of 13.4 ppm in the rock formation. The shape of the ratio curves can be understood by referring to Fig. 11, which shows the fraction of the total cross section contributed by the Compton, photoelectric, and pair production processes as a function of gamma-ray energy for a sandstone formation having zero porosity and saturation (dry, nonporous rock). The photoelectric effect plays a prominent role only below ~200 keV. In ONETRAN, the photoelectric effect is treated as an absorption channel that simply removes photon flux. Thus, the shape of the flux ratio curve at low energies depends on the relative magnitude of the photoelectric cross section for the formations being compared.[3,4]

The shape of the flux ratio curve at energies above ~2 MeV is influenced by the relative magnitude of the pair production cross section for the formations being compared. However, the dependence is much weaker than that observed for the photoelectric effect because the Z of the formation is low (~11). Hence, the pair production cross section contributes only ~5% to the total cross section at 3 MeV. In Fig. 10, this effect produces a very

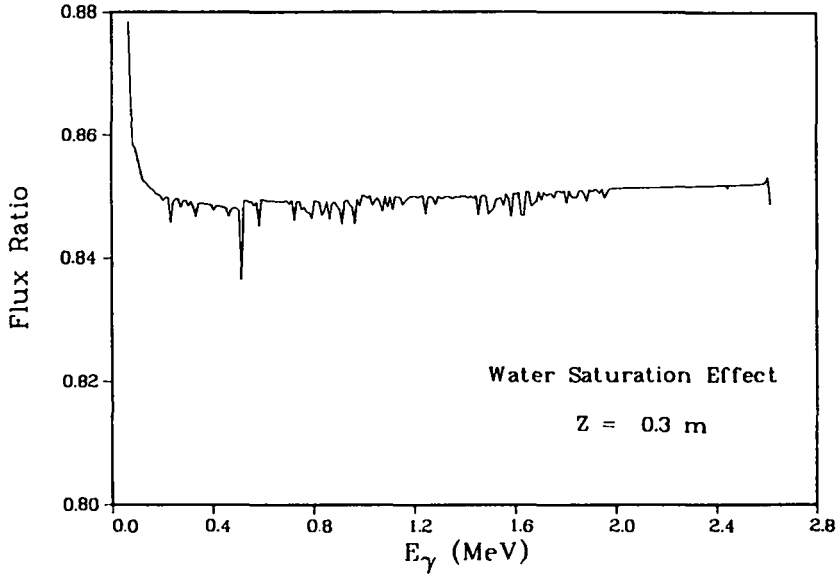

Fig. 9. Ratio of gamma-ray total flux at a survey height of 0.3 m (1 ft) for rock formations containing a 13.4-ppm thorium source and differing only in water saturation (S = 1.0 vs S = 0.0).

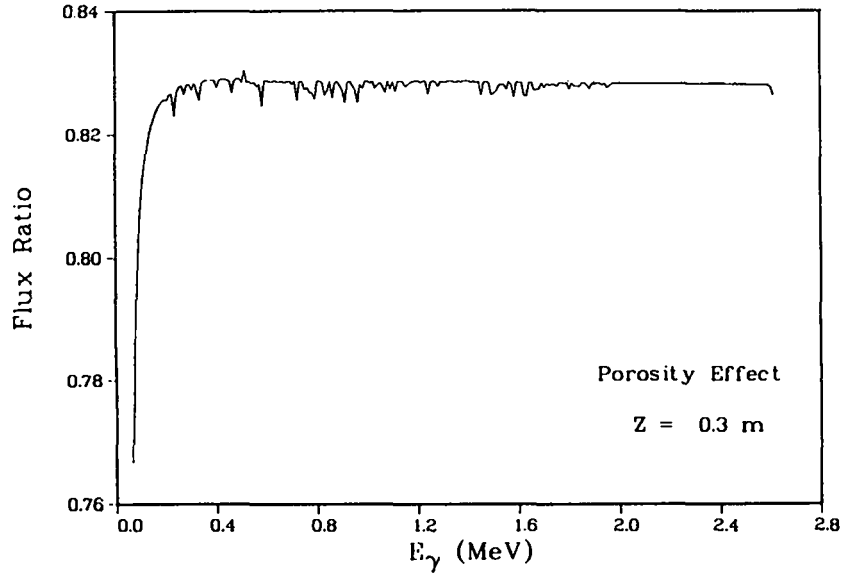

Fig. 10. Ratio of gamma-ray total flux at a survey height of 0.3 m (1 ft) for rock formations containing a 13.4-ppm thorium source and differing only in formation porosity (P = 0.1 vs P = 0.3).

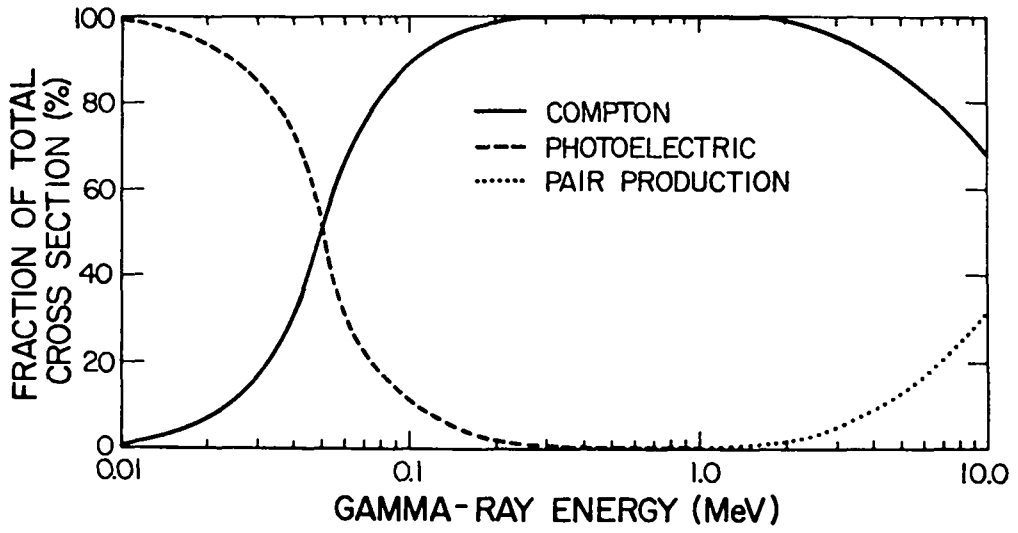

Fig. 11. Fractional contributions of the Compton, photoelectric, and pair production interactions to the total cross section of a dry, nonporous sandstone formation having a bulk density of 2.6263 g/cm^3.

slight droop in the flux ratio above ∿2 MeV that is barely discernible in the figure but is readily apparent in a listing of the flux ratio values.

The Compton cross section accounts for more than 98% of the total cross section between ∿200 keV and 2 MeV, giving rise to the flat region of the flux ratio curves. It can be shown[11] that, for a homogeneous infinite medium containing a uniformly distributed source, the uncollided total flux ψ_u at any point in the medium is given by $\psi_u = Q/\sigma$, where Q is the source concentration and σ is the macroscopic total cross section for the medium at the source energy. However, this relationship is true only for the highest energy source line in the spectrum. At lower energies, the total flux consists of scattered radiation and lower energy source lines. For these energies, the relationship is approximately valid, as the scattered component of the flux can be thought of as originating from secondary sources within the medium.

It also can be demonstrated[8] that the radiation field above a homogeneous semi-infinite medium containing uniformly distributed sources is directly proportional to the source concentration and inversely proportional to the total cross section: $\psi \propto Q/\sigma$. In the energy region dominated by Compton scattering (that is, 200 keV-3 MeV), the total flux is approximately inversely

proportional to the macroscopic Compton cross section σ_c for the rock medium: $\psi \sim Q/\sigma_c$. But

$$\sigma_c \propto \Sigma_i \rho'_i Z_i \quad ,$$

where Z_i is the atomic number of the i^{th} element of the formation, and the atomic density ρ_i of the i^{th} element can be written

$$\rho'_i \equiv \rho_i A_v/A_i \quad ,$$

where A_v is Avogadro's number, ρ_i is the mass density of the i^{th} element, and A_i is the atomic mass of the i^{th} element. Thus, the Compton cross section is proportional to

$$\sigma_c \propto \Sigma_i \rho_i(Z_i/A_i) \equiv \overline{Z/A} \quad ,$$

where the summation is simply the mass-density-weighted value of $\overline{Z/A}$ for the formation. Then we have

$$\psi \approx Q/\overline{Z/A} \quad ,$$

so that the ratio of total flux for differing formations is inversely proportional to the ratio of $\overline{Z/A}$ for the formations.

This relationship is demonstrated in Table VIII, where ONETRAN total flux ratios are compared with inverse $\overline{Z/A}$ and inverse σ. The first comparison is between cases having identical porosity (P = 0.3) but different water saturation: the formation of Case 7 is completely dry (S = 0.0), whereas that of

TABLE VIII

RATIOS OF FORMATION PARAMETERS

Formations Compared	Inverse[a] $\overline{Z/A}$	Inverse[b] σ	ONETRAN Total Flux
(P = 0.3,S = 1.0)/(P = 0.3,S = 0.0)	0.8462	0.8462	0.8472
(P = 0.1,S = 0.5)/(P =0 .3,S = 0.5)	0.8289	0.8292	0.8281

[a]Mass-density-weighted $\overline{Z/A}$.
[b]Total macroscopic cross section at 1.0 MeV.

Case 9 is fully saturated (S = 1.0). The energy dependence of the total flux ratio (Case 9/Case 7) is shown in Fig. 9. Both the inverse value of $\overline{Z/A}$ and the inverse σ accurately predict the flux ratio in the Compton region (200 keV-3 MeV), especially when one considers that the ONETRAN flux values are computed to a precision of 0.1%.

The second comparison in Table VIII is between cases having the same saturation (S = 0.5) but different porosities (P = 0.1 and P = 0.3). The energy dependence of the total flux ratio (Case 11/Case 8) is shown in Fig. 10. Again, both the inverse formation $\overline{Z/A}$ and σ accurately predict the flux ratio in the flat Compton region of the curve. The apparent "structure" in the total flux ratios is real and is associated with the thorium source lines and the relative amount of flux downscattered into a given bin from higher energy bins and the flux scattered from the bin to lower energies or absorbed.[12]

B. Dependence of the Total Flux on the Density/Altitude of the Air

The variation of total flux spectra with survey height is demonstrated in Fig. 12, wherein the total flux at 121.9 m (400 ft) is compared with that at 0.3 m (1 ft) as a function of gamma-ray energy. The formation porosity, saturation, density, composition, etc., are held constant, and a thorium dry weight concentration of 13.4 ppm is assumed (Case 8). The chief effect of increasing

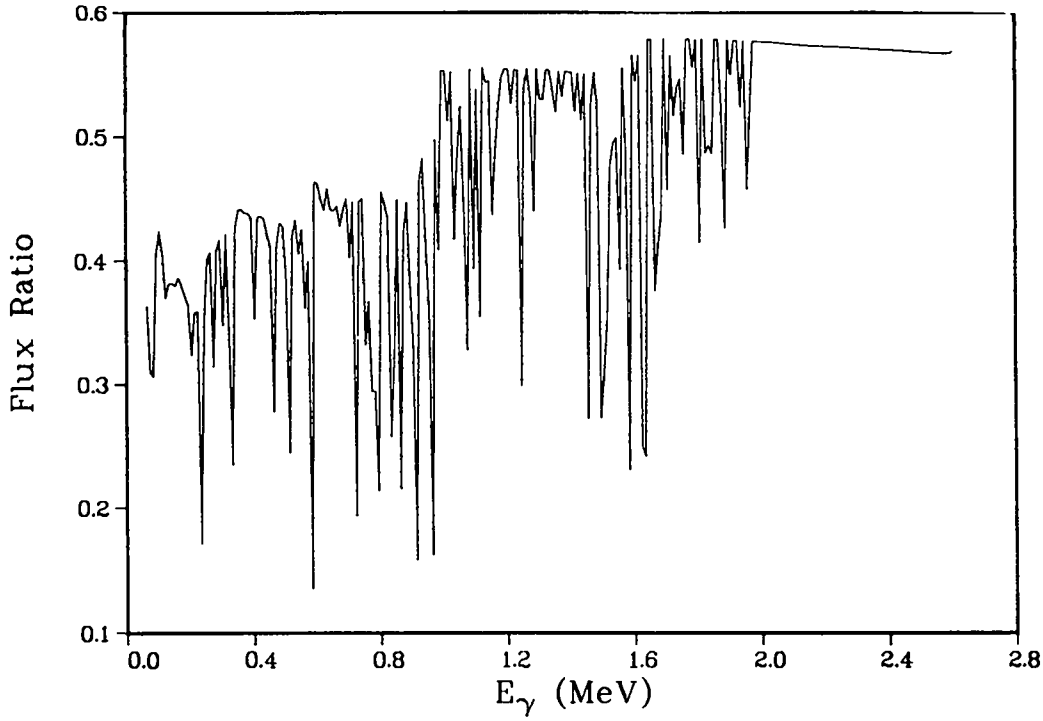

Fig. 12. Ratio of gamma-ray total flux at a survey height of 121.9 m (400 ft) to that at 0.3 m (1 ft). All other parameters were held constant including the thorium source strength.

survey height is that of increasing spectral attenuation. However, the attenuation is not uniform and depends on the energy and the presence of lines in the source spectrum. A monoenergetic source would yield a flux ratio curve that would be relatively flat in the Compton region (200 keV-2 MeV) and would exhibit a sharp falloff in the photoelectric region ($\sim$200 keV) because of the increased photoelectric absorption at 121.9 m as compared with that at 0.3 m. These general features are apparent in the flux ratio curve of Fig. 12 as well. The flat region between about 2 and 2.6 MeV indicates that $\sim$44% of the flux in that region at 0.3 m is downscattered to lower energies at 121.9 m. The increased photoelectric absorption at the higher survey height results in the flux ratio tending lower at the lower energies. However, structure appears in the ratio as discrete dips superimposed on a step function that increases in magnitude with increasing energy. This structure is real and results from differing amounts of flux being downscattered into and out of each energy bin because of the interplay between the presence of discrete lines in the source spectrum and the various gamma-ray interaction mechanisms. The same effect is

apparent in Figs. 9 and 10 but is much reduced because the difference in absorption for these comparisons is much smaller than that owing to the air medium between 0.3 and 121.9 m for Fig. 12.

The dependence of the total flux spectrum on the density/altitude of the air medium has also been investigated. The flux ratio between cases having the same density/altitude product but different values of altitude and air density is shown in Fig. 13. The formation parameters (porosity, saturation, density, etc.) were held constant, and the total flux at 1.811×10^4 cm (594.2 ft) in air having a constant (sea level) density $\rho = 1.205 \times 10^{-3}$ g/cm^3 was compared with the total flux at 2.438×10^4 cm (800 ft) in air having a constant density corresponding to an altitude of 8000 ft ($\rho = 8.95 \times 10^{-4}$ g/cm^3).

The total flux ratio of Fig. 13 demonstrates that spectra obtained at identical values of density/altitude generally have different spectral shapes. If the total flux depended only on Compton scattering, the total flux ratio would be a constant unity value for all energies. However, the flux depends on three photon interactions, not just one, resulting in the structure that is apparent in the figures. Also apparent in Fig. 13 is the nonunity level of the flat Compton region of the ratio curve. This discrepancy indicates that the flux at a given value of density/altitude may depend on factors other than those related to photon absorption. Close examination of the curves of Fig. 14 sheds light on this dependence.

The curves of Fig. 14 demonstrate the attenuation of the total flux with survey height for two energy bins of the thorium spectrum of Case 2. The upper curve is typical of energy bins containing only unscattered flux, whereas the lower curve shows the dependence of bins containing only scattered flux (no source lines). Simple exponential attenuation would result in a perfectly linear dependence on a semilogarithmic plot. The lower curve appears to be nearly linear, but the upper curve is nonlinear especially for survey heights below about 100 m.

The same effect causes both the nonlinearity observed for the unscattered flux and the variation of the angular flux with survey height observed previously (Sec. III.B). The unscattered flux at a given height comprises infinitely many components, each component representing the contribution to the total flux from the "circles of investigation" surrounding the observation point. As the survey height changes, the relative contribution from each

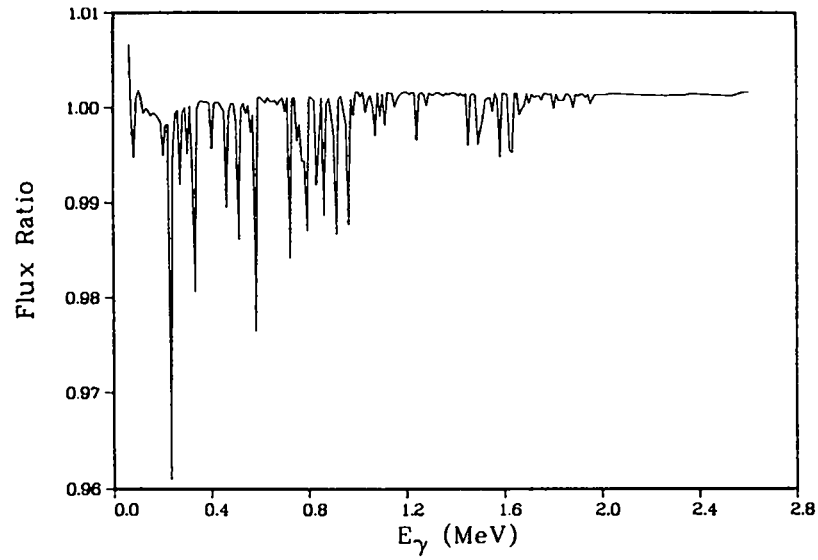

Fig. 13. Ratio of gamma-ray total flux for surveys having identical values of density/altitude product but different values of air density and altitude ($z = 1.811 \times 10^4$ cm, $\rho = 1.205$ mg/cm^3 vs $z = 2.438 \times 10^4$ cm, $\rho = 0.895$ mg/cm^3).

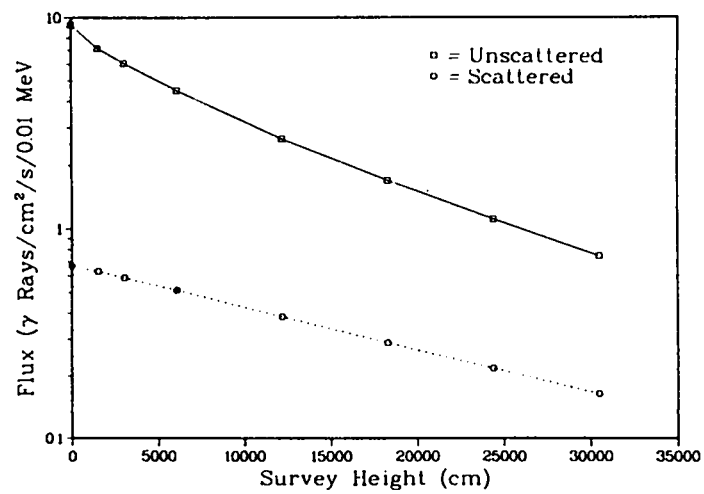

Fig. 14. Variation of gamma-ray total flux with survey height for energy bins containing either only unscattered flux or only scattered flux. The rock formation had a porosity of 0.3, a saturation of 0.5, and a thorium dry weight concentration of 13.4 ppm.

circle varies, resulting in the nonexponential attenuation of the total flux with height.

The nearly perfect exponential dependence of the scattered flux with height can be qualitatively understood in terms of the circles of investigation as well. Photons emitted from a given circle can scatter one or more times and pass through the observation point at angles of incidence that are characteristic of photons emitted from neighboring circles and passing through the observation point unscattered. Contributions of the circles of investigation mix; hence, a more nearly isotropic angular dependence of the scattered flux results. Thus, as the survey height increases, the primary effect observed for the scattered flux is that resulting from increasing exponential attenuation. Geometrical effects play a greatly diminished role in the variation of total flux with survey height.

The flux in energy bins containing both scattered and unscattered contributions displays a dependence with survey height that varies, of course, with the relative strength of the two contributing fluxes. This mixing of scattered and unscattered fluxes greatly complicates spectral-log interpretation. Thus, a simple density/altitude correction cannot be applied to a spectral log to eliminate all the differences in altitude and air density between the field log and calibrated log. Spectral shape differences would persist, especially below $\sim$1 MeV (for the thorium spectrum). However, this correction would be in error by only 1% in the KUT energy region ($\sim$1.2-2.8 MeV) and might prove adequate for most spectral KUT aerial logging applications.

V. CONCLUSIONS

These results lead to the following conclusions regarding the effects on total flux spectra observed at a fixed height above a semi-infinite source-bearing medium.

(1) Variations in formation porosity or saturation (and implicitly in formation effective Z and density) cause little spectral shape change above about 200 keV.

(2) Formation effective Z might be determined from spectral shape variations below 200 keV.

(3) If the formation effective $\overline{Z/A}$ can be determined independently, the spectral log can be corrected easily to yield quantitative information on source concentration (assuming secular equilibrium in the uranium and thorium decay series).

Similar conclusions have been drawn previously concerning the total flux spectra observed in infinite media containing uniformly distributed sources.[3,4]

In addition, the following conclusions can be drawn concerning the variation of total flux spectra as a function of height above the rock/air interface and the density/altitude of the air medium for fixed formation parameters (porosity, saturation, density, etc.).

(1) The spectral shape of the total flux depends strongly on the height above the formation surface. This fact in turn implies that the KUT stripping parameters will be sensitive to small variations in survey height and must be determined as a function of survey height.

(2) Corrections to the total flux spectra for changes in the density of the air and the elevation of the formation surface can be made by simple scaling with density/altitude. This correction would not remove all spectral shape differences, especially those below $\sim$1 MeV. However, as a practical matter, the density/altitude correction would be in error by only $\sim$1% for the KUT energy region and should prove adequate for most spectral KUT aerial logging applications.

REFERENCES

1. M. L. Evans, "A Computer Model for Calculating Gamma-Ray Pulse-Height Spectra for Logging Applications," 50th Annual International Meeting of the Society of Exploration Geophysicists, Houston, Texas, 1980.

2. T. R. Hill, "ONETRAN: A Discrete Ordinates Finite Element Code for the Solution of the One-Dimensional Multigroup Transport Equation," Los Alamos Scientific Laboratory report LA-5990-MS (June 1975).

3. Mahavir Jain, M. L. Evans, and D. A. Close, "Nondestructive Assay Technology for Uranium Resource Evaluation Infinite Medium Calculations, Final Report," Los Alamos Scientific Laboratory report LA-7713-MS (March 1979).

4. M. L. Evans, D. A. Close, and M. Jain, "Transport of Gamma Rays Through an Infinite Homogeneous Ore Medium," Nucl. Instrum. and Methods 192, 583 (1982).

5. Nuclear Data Sheets, B5, No. 1 (1971); 8, No. 2 (1972); 17, No. 3 (1976); 20, No. 2 (1977); 21, No. 1 (1977); and 21, No. 4 (1977).

6. C. Lederer and V. Shirley, Table of Isotopes (John Wiley & Sons, Inc., New York, 1978), 7th Ed.

7. H. L. Beck, "Absolute Intensities of Gamma Rays From the Decay of ^{238}U and ^{232}Th, New York Operations Office, Atomic Energy Commission, Health and Safety Laboratory report HASL-262 (1972).

8. L. Lovborg and P. Kirkegaard, "Numerical Evaluation of the Natural Gamma Radiation Field at Aerial Survey Heights," Riso Report No. 317 (1975).

9. E. D. Cashwell, J. R. Neergaard, C. J. Everett, R. G. Schrandt, W. M. Taylor, and G. D. Turner, "Monte Carlo Photon Codes: MCG and MCP," Los Alamos Scientific Laboratory report LA-5157-MS (March 1973).

10. J. S. Duval, B. Cook, and J. A. S. Adams, "Circle of Investigation of an Airborne Gamma-Ray Spectrometer," J. Geophys. Res. 76, 8466-8470 (1971).

11. G. Bell and S. Glasstone, Nuclear Reactor Theory (Van Nostrand Reinhold, New York, 1970).

12. D. A. Close, M. L. Evans, and M. Jain, "Gamma-Ray Spectral Calculations for Uranium Borehole Logging," Los Alamos Scientific Laboratory report LA-8417-MS (June 1980).

Printed in the United States of America
Available from
National Technical Information Service
US Department of Commerce
5285 Port Royal Road
Springfield, VA 22161

Microfiche (A01)

Page Range	NTIS Price Code	Page Range	NTIS Price Code	Page Range	NTIS Price Code	Page Range	NTIS Price Code
001-025	A02	151-175	A08	301-325	A14	451-475	A20
026-050	A03	176-200	A09	326-350	A15	476-500	A21
051-075	A04	201-225	A10	351-375	A16	501-525	A22
076-100	A05	226-250	A11	376-400	A17	526-550	A23
101-125	A06	251-275	A12	401-425	A18	551-575	A24
126-150	A07	276-300	A13	426-450	A19	576-600	A25
						601-up*	A99

*Contact NTIS for a price quote.

Los Alamos